Continental Stratus Clouds: A Case Study Using Coordinated Remote Sensing and Aircraft Measurements

KENNETH SASSEN, GERALD G. MACE, AND ZHIEN WANG

Department of Meteorology, University of Utah, Salt Lake City, Utah

MICHAEL R. POELLOT

Atmospheric Sciences Department, University of North Dakota, Grand Forks, North Dakota

STEPHEN M. SEKELSKY AND ROBERT E. MCINTOSH*

Microwave Remote Sensing Laboratory, University of Massachusetts–Amherst, Amherst, Massachusetts

(Manuscript received 12 December 1997, in final form 11 August 1998)

ABSTRACT

A continental stratus cloud layer was studied by advanced ground-based remote sensing instruments and aircraft probes on 30 April 1994 from the Cloud and Radiation Testbed site in north-central Oklahoma. The boundary layer structure clearly resembled that of a cloud-topped mixed layer, and the cloud content is shown to be near adiabatic up to the cloud-top entrainment zone. A cloud retrieval algorithm using the radar reflectivity and cloud droplet concentration (either measured in situ or deduced using dual-channel microwave radiometer data) is applied to construct uniquely high-resolution cross sections of liquid water content and mean droplet radius. The combined evidence indicates that the 350–600 m deep, slightly supercooled (2.0° to −2.0°C) cloud, which failed to produce any detectable ice or drizzle particles, contained an average droplet concentration of 347 cm^{-3}, and a maximum liquid water content of 0.8 g m^{-3} and mean droplet radius of 9 μm near cloud top. Lidar data indicate that the K_a-band radar usually detected the cloud-base height to within ~50 m, such that the radar insensitivity to small cloud droplets had a small impact on the findings. Radar-derived liquid water paths ranged from 71 to 259 g m^{-2} as the stratus deck varied, which is in excellent agreement with dual-channel microwave radiometer data, but ~20% higher than that measured in situ. This difference appears to be due to the undersampling of the few largest cloud droplets by the aircraft probes. This combination of approaches yields a unique image of the content of a continental stratus cloud, as well as illustrating the utility of modern remote sensing systems for probing nonprecipitating water clouds.

1. Introduction

Although marine stratus clouds have recently been the subject of major field projects such as in the First International Satellite Cloud Climatology Program Regional Experiment (FIRE), including the stratus of both the eastern Pacific (Albrecht et al. 1988) and Atlantic (Albrecht et al. 1995) Oceans, continental stratus clouds have been comparatively overlooked despite their relative accessibility (Del Genio et al. 1996). Such boundary layer clouds are known to significantly affect the surface heat budget and are probably important modulators of our climate because of their high albedos. It can be expected that geography will have a large impact on stratus cloud properties as a result of two factors: variations in the source and abundance of cloud condensation nuclei (CCN), and, indirectly, the fundamental dependence on temperature of the adiabatic release rate of the condensate (Sassen et al. 1992; Gultepe and Isaac 1997). The resultant variations in the cloud droplet concentration N_d, mean radius $\bar{r}$, liquid water content (LWC), and vertically integrated liquid water path (LWP) have important radiative consequences. As a result of this diversity in cloud content and the difficulties inherent in characterizing them with satellites, stratus clouds are still a poorly understood component of the planet's radiation balance, as has been recognized in the design of Project FIRE. Moreover, water cloud alterations caused by pollution-induced changes in droplet spectra have long been hypothesized as a mechanism for climate change (Twomey 1974; Slingo 1990), al-

* Deceased.

Corresponding author address: Kenneth Sassen, 135 S. 1460 E. (819 WBB), University of Utah, Salt Lake City, UT 84112.
E-mail: ksassen@atmos.met.utah.edu

© 1999 American Meteorological Society

Unauthenticated | Downloaded 03/29/23 10:44 AM UTC

though they may be more important in the case of maritime clouds because of their lower droplet concentrations (Kogan et al. 1996).

In comparison to marine stratus clouds, which form with the aid of relatively large ocean-derived CCN, their continental counterparts generally contain greater concentrations of smaller droplets due to the more numerous terrestrial CCN activated in updrafts (see, e.g., Hanel 1972; Martin et al. 1994). Hence, continental stratus clouds tend to produce narrower cloud droplet size distributions, which are more colloidally stable and so less likely to produce drizzle through the droplet coalescence process. The dynamics of both the oceanic and continental varieties of these clouds, though, are essentially the same; they occur at the top of well-mixed boundary layers capped by temperature inversions (Martin et al. 1994). The stratus cloud system described here exemplifies these attributes of continental boundary layer clouds.

A modern aspect of the study of water clouds in general, and stratus clouds in particular, has been an increasing reliance on remote sensing information to characterize their microphysical contents and structures. Microwave radars employing millimeter wavelengths have been shown to be well suited for probing nonprecipitating water clouds because of their sensitivity to relatively small cloud droplets (Pasqualucci et al. 1983; Lhermitte 1987; Mead et al. 1994). To realize the potential of radar for remotely deriving cloud properties like liquid water content, cloud retrieval algorithms based on a variety of techniques have been developed (Atlas 1954; Frisch et al. 1995; Sauvageot and Omar 1987; Liao and Sassen 1994; Sassen and Liao 1996). In addition, the development of dual-channel microwave radiometers (Hogg et al. 1983) for sensing the vertically integrated amounts of cloud liquid water also represents a major improvement in water cloud research capabilities, and hybrid active/passive microwave remote sensing methods appear to be particularly promising for inferring cloud contents (Frisch et al. 1995).

The case study described here is based on coordinated remote sensing and aircraft operations collected during the April 1994 remote cloud sensing intensive observation period (RCS IOP) at the Atmospheric Radiation Measurement Clouds and Radiation Testbed (CART) site near Lamont, Oklahoma (Stokes and Schwartz 1994). Presented are measurements collected by the University of Massachusetts Cloud Profiling Radar System (CPRS), the University of Utah Polarization Diversity Lidar (PDL), and the University of North Dakota Citation aircraft, as well as additional permanent CART instrumentation. The goal of the RCS IOP field campaign was to provide closely coordinated air-truth cloud microphysical data for the testing of remote sensing cloud retrieval algorithms under various conditions; on 30 April this field experiment provided a unique opportunity to better understand the composition and structure of a continental stratus cloud system. In this paper we demonstrate the utility of this combination of state-of-the-art remote sensors for deriving quantitative data from nonprecipitating water clouds, employing the cloud property retrieval algorithms described below.

2. The dataset

a. Cloud system

The stratus clouds studied on the afternoon of 30 April 1994 were associated with a widespread springtime cold-air outbreak over the central United States. Figure 1 shows the regional (a) infrared and (b) visible channel *GOES-7* satellite views of the stratus cloud conditions at 2100 (all times are given in UTC). The stratus cloud outbreak can be seen to be extensive, covering most of the southern and northeastern Great Plains. A rather uniform-appearing cloud mass is present locally at the CART site (the dot in north-central Oklahoma), although breaks in the cloud deck are approaching from the north. The thinner stratus clouds to the southeast are more broken and cellular, forming a series of cloud bands approximately orthogonal to the northwesterly flow.

The broad area of stratus clouds evident in Fig. 1 formed in a region of strong low-level cold-air advection behind a vigorous cold front that extended from the Texas Gulf coast into the Ohio Valley by the afternoon of 30 April. The cold pool at 850 mb was centered over Nebraska ($T_{850} = -5$°C) with the temperature gradient extending across Oklahoma to the front, where $T_{850} =$ 14°C. Aloft, the axis of the 500-mb shortwave trough passed over the CART site just after 1200 on 30 April, leading to negative vorticity advection in the weak northwesterly flow. The conjunction of cold-air advection and negative vorticity advection suggest strong subsidence in the free troposphere during the study period. Due to heavy rain associated with the frontal passage and thunderstorms ahead of the front, ample surface moisture was available for cloud formation in the boundary layer.

Given in Fig. 2 are profiles of boundary layer temperature, equivalent potential temperature, and relative humidity (with respect to water), collected during the initial slow spiral ascent of the University of North Dakota (UND) Citation over the CART site from 2031 to 2045. Clearly, the structure of the boundary layer is that of a cloud-topped well-mixed layer bounded by a strong temperature inversion similar to that reported for marine stratocumulus clouds (Brost et al. 1882; Albrecht et al. 1985, 1988; Martin et al. 1994).

b. Instrumentation

The specifications of the two active remote sensing systems supporting this case study are given in Table 1. The CPRS has simultaneous dual-wavelength (K_a and W band), Doppler, linear depolarization, and differential

Unauthenticated | Downloaded 03/29/23 10:44 AM UTC

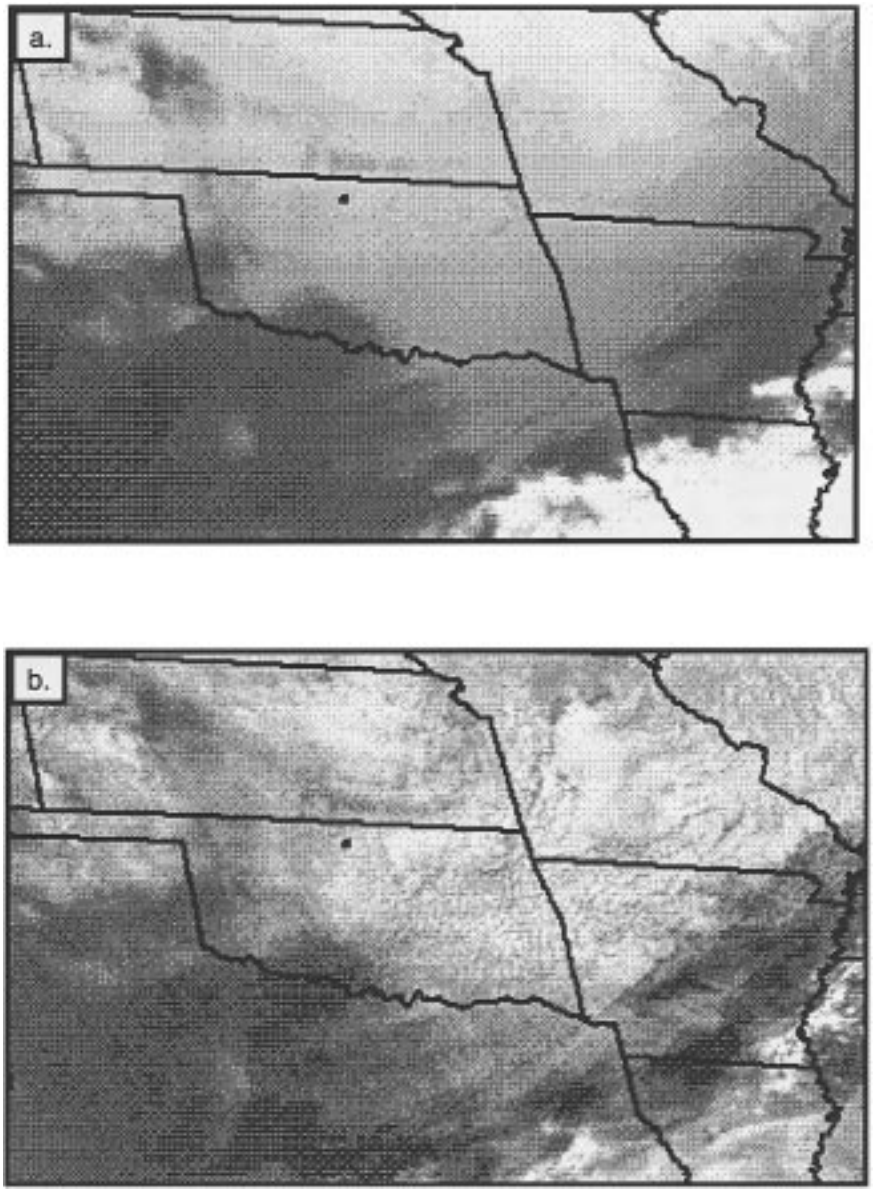

FIG. 1. Central United States (a) infrared 10-km and (b) visible 1-km resolution satellite images showing the extent of the stratus cloud outbreak at 2100 UTC on 30 April 1994.

reflectivity measurement capabilities (Mead et al. 1994). The four-channel PDL also has dual-wavelength and linear depolarization capabilities, and exceptional high spatial and temporal resolutions (Sassen 1994). Although both units are fully scannable and both collected dual-wavelength data on this occasion, only vertically pointing single (9.05 mm and 1.06 μm) wavelength and radar Doppler data are presented here over the initial period of aircraft operations from 2030 to 2200. Since relatively small spherical scatterers were exclusively present in the stratus, the additional measurement capabilities do not provide significant additional insights with respect to our current objectives. The K_a-band radar data are used here because the single-antenna design of the CPRS provides ~3 dB more gain at the 9.05-mm wavelength.

In addition to these mobile instruments, regularly operated CART devices also called upon to enhance this study include a dual-channel microwave radiometer MWR, and special CART soundings. Note that the physical separation of the three main instruments, the MWR, PDL, and CPRS at the CART site ranged from ~50 m (between the former) to 250 m; these instruments were distributed along a radial of ~15°, compared to the mean stratus cloud wind direction of 340° (at 9 m s^{-1}). The vertically integrated liquid water depth data measured by the MWR are subject to two kinds of uncertainties, which result from gradual drifts in calibration and dif-

Unauthenticated | Downloaded 03/29/23 10:44 AM UTC

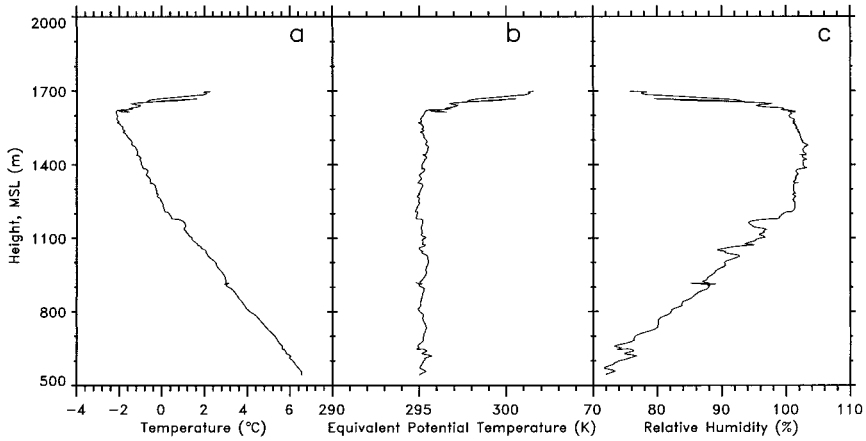

FIG. 2. Profiles of temperature, equivalent potential temperature, and relative humidity obtained by the UND Citation during the initial spiral ascent (2030–2045) above the CART site.

ferences between the assumed (i.e., climatological) and actual water cloud temperatures. In this study, although the former is difficult to determine accurately due to the ~48-h duration of the cloud event, the MWR calibration drift does not appear to be significant, and the ~0°C midcloud temperature was very close to the statistical April cloud temperature average (J. C. Liljegren 1998, personal communication).

The UND Citation operations over the entire 2030–2315 mission were designed to closely support the ground-based remote sensing observations. (In this report, we concentrate on the 2030–2200 period supported by radar data.) In the case of this relatively thin stratus layer, the operations consisted of a series of slow and rapid ascent/descent ramps (~2.5 and 10 m s^{-1}, respectively) through the cloud layer, along with three constant-level legs from 2246 to 2301, and slow spirals (of ~10-km radius) within the stratus centered above the CART site at the beginning and end of the mission. The ramps, which were also centered over the CART site, averaged 16 km in length and were conducted at headings of ~345° and 165°, along the mean cloud-level winds.

The in situ instrumentation relied on here to describe the content of the cloud are the laser-based forward scattering spectrometer probe (FSSP) for cloud droplet sizing (in 15 diameter bins between 2.8 and 54.2 μm with account for aircraft sampling effects) and LWC calculation, and the King heated-wire probe for independent LWC measurement. Note that essentially no 2D-C particle images (or zero-area image counts) for water or ice phase particles larger than the 33-μm threshold diameter were recorded during the mission. In other words, precipitation-sized water or ice particles, if present, were too scarce to be detected with these standard instruments.

c. The remote sensing algorithm

A previously developed water cloud retrieval algorithm for K_a-band radar (Liao and Sassen 1994) is applied here to derive the LWC field within the stratus layer. This method relies on the following equation, developed through a regression analysis of findings from a 1D adiabatic water cloud model (Sassen et al. 1992) under a large variety of microphysical and environmental situations, including characteristic maritime and continental CCN size distributions (from Hanel 1972) and concentrations (100–1000 cm^{-3}), updraft velocity (0.1–1.0 m s^{-1}), and temperature (20° to −10°C):

$$Z_e = (3.6/N_d)\mathrm{LWC}^{1.8}. \quad (1)$$

TABLE 1. Specifications of the CPRS and PDL systems. Here V + H and (V + H) refer to the vertical and horizontal polarization transmitted (received).

	CPRS		PDL	
Wavelength	9.06 mm	3.16 mm	1.06 μm	0.532 μm
Peak power	1.2×10^5 W	1.5×10^3 W	4.4×10^7 W	3.5×10^7 W
Pulse repetition frequency	0.2–3.0 kHz	1 Hz–20 kHz	10 Hz	10 Hz
Pulse width	0.2–2.0 μs	0.05–2.0 μs	9.0 ns	9.0 ns
Resolution	30 m	30 m	1.5 m	1.5 m
Beamwidth	0.6° (3 dB)	0.2° (3 dB)	0.5 mrad	0.5 mrad
Diameter	1.0-m lens	1.0-m lens	0.3 m	0.3 m
Noise figure	11 dB	13 dB	N/A	N/A
Polarization	V or H (V + H)	V or H (V + H)	H (V + H)	H (V + H)

Unauthenticated | Downloaded 03/29/23 10:44 AM UTC

Clearly, to derive LWC from Z_e via this approach it is necessary to have knowledge of N_d, a potentially highly variable quantity that depends on the local CCN activity spectrum (i.e., on airmass source and history). This dependency results from water vapor competition effects among the growing droplets, which serve to limit the sizes of the largest and most strongly Rayleigh-scattering droplets in relation to the essentially constant adiabatic liquid water release rate supplied at a given temperature. It is also necessary to assume in the retrieval that N_d is constant with cloud height for each radar cloud profile treated.

On the other hand, the reliance of this method on knowledge of N_d to accurately determine LWC from Z_e can be overcome through the use of coincident LWP information provided by an MWR. From Eq. (1) and the definition of LWP, we have

$$N_d = 3.6(\mathrm{LWP}/\Delta z)^{1.8} \Big/ \sum_{z_{cb}}^{z_{ct}} Z_e, \qquad (2)$$

where Δz is the cloud depth and the summation of Z_e is from the cloud-base z_{cb} to cloud-top z_{ct} heights.

Finally, with knowledge of the radar-derived LWP and N_d, it is straightforward to compute a measure of the mean cloud droplet radius using the following definition:

$$\bar{r} = (3\mathrm{LWC}/4\pi\rho N_d)^{1/3}. \qquad (3)$$

It should be noted that although the model framework is based on the adiabatic process, the violation of this process does not necessarily invalidate the radar algorithm. Model tests show that a decrease in the LWC profile caused by mixing with dry air in an updraft does not significantly affect the Z_e–LWC relation, although it should be acknowledged that other mixing processes such as the introduction of new droplets grown from unactivated CCN and the effects of selective droplet evaporation at cloud boundaries cannot be evaluated with a 1D model. In essence, this and similar LWC algorithms rely on the assumption of a characteristic mean width to the droplet size distribution (in order to specify the relation between the third and sixth moments of the size distribution): in our case this width is inherently treated within the model framework based on the initial distribution of dry CCN masses, and their subsequent growth history.

3. Overview of in situ findings

To illustrate the cloud microphysical contents measured during the 15 individual aircraft flight segments of interest here, and their variability, Figs. 3a,b provide vertical LWC and N_d profiles derived from the FSSP, and Table 2 compiles the corresponding cloud microphysical content in terms of the vertically integrated LWP and ramp-averaged N_d. (The latter values in Table 2 are calculated only for LWC ≥ 0.1 g m^{-3} in order to avoid undercounting problems when small droplets dominate near cloud boundaries: a ~6% decrease in average N_d occurs when LWC > 0 are considered.) The FSSP LWC (dashed lines in Fig. 3a) and N_d profiles are based on 30-m vertical averages matching the vertical resolution of the radar to improve the comparison with the LWC profiles derived over the corresponding periods using the radar retrieval algorithm of Eq. (1) (solid lines). Note that on average the N_d profiles in Fig. 3b (for LWC > 0 g m^{-3}) are nearly constant with height, except near the cloud boundaries where small drops dominate, thus supporting the constant N_d theoretical assumption. Also included in Fig. 3a are the lowest 30-s average cloud-base heights measured by the lidar over each period (arrows), and at top are the flight segment designations (see Table 2).

It is apparent from Fig. 3 and Table 2 that the stratus layer properties varied a good deal during the conduct of the aircraft operations. To facilitate the intercomparison of the remote and in situ data, then, some temporal averaging of the data may prove useful, as we attempt in Fig. 4. In this figure LWC profiles from the FSSP (solid line), King probe (dashed line), and radar algorithm (line with dots) have been averaged over the five middle aircraft ramps (R5–R9). These five ramps are considered the most reliable because the aircraft did not sample the relatively high cloud tops sensed by the radar during the first four ramps (R1–R4), while the four fast ramps (FR1–FR4) may have been affected by potential droplet sampling problems related to the reduced cloud volumes probed at the higher ascent/descent rates (see appendix A). Ignoring for the moment the radar-derived data, it can be seen that the FSSP and King LWC data are in reasonable agreement, considering that the two probes work on very different principles (i.e., laser scattering vs heated wire resistance).

Finally, provided in Fig. 5 is a typical example of the change with height in the FSSP-derived droplet size distributions from ramp R7, showing the cloud evolution in 30-m average height intervals from cloud base to 510 m above cloud base. This plot reveals the gradual vertical increase in cloud droplet sizes until a sudden decrease in small-particle concentrations occurs near the cloud top in response to the effects of dry-air entrainment. As described in appendix A, FSSP limitations in detecting low concentrations of cloud droplets under the conditions imposed by the Citation flight patterns have implications for the accurate assessment of LWC.

4. Remote sensing cloud images

Provided in Fig. 6 are high-resolution remote sensing data records over the 2030–2200 period of CPRS K_a-band radar observations. Shown are height versus time displays of (a) effective radar reflectivity factor Z_e (mm^6 m^{-3}), where lidar cloud-base heights are shown by the solid line; (b) PDL relative 0.532-μm backscattering; (c) mean vertical Doppler velocity V (m s^{-1}); and (d)

Unauthenticated | Downloaded 03/29/23 10:44 AM UTC

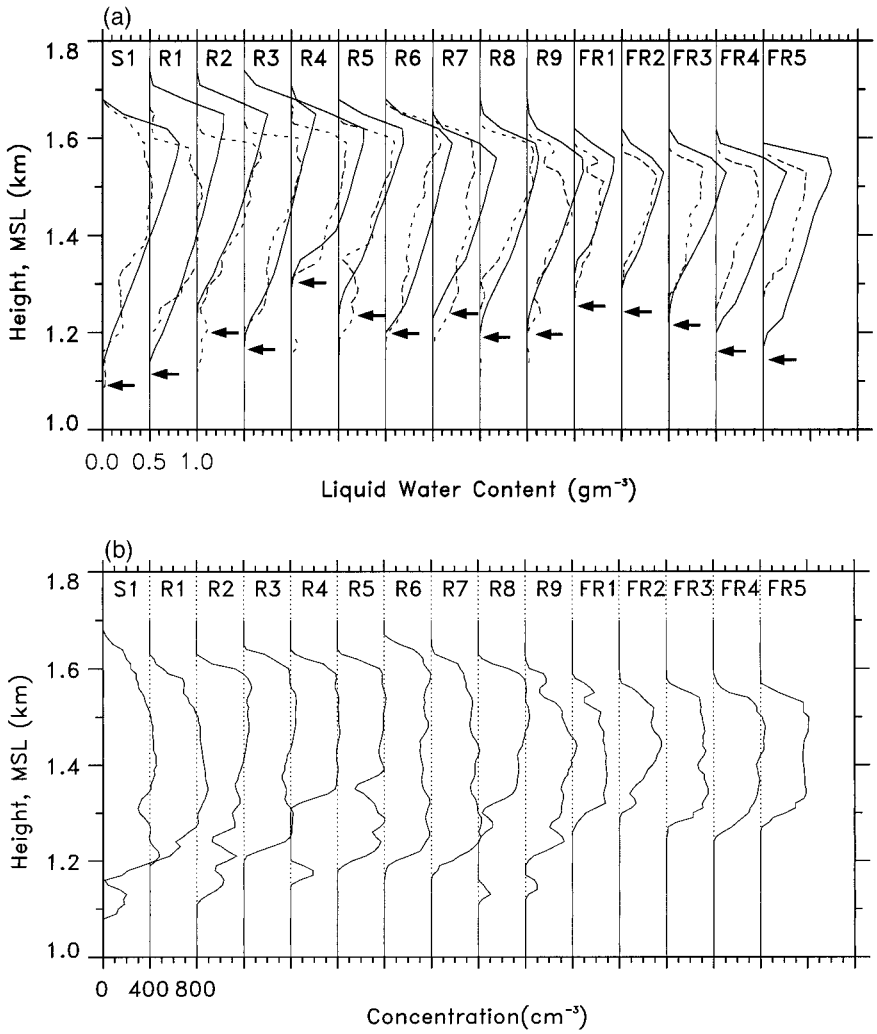

FIG. 3. Comparison of vertical profiles of (a) LWC derived from the FSSP (dotted) and the radar algorithm (solid) using the average in situ measured N_d, with arrows indicating the lidar cloud-base height; (b) the FSSP-derived droplet number concentration. Each set of profiles in (a) [or (b)] is shifted to the right by 0.5 gm^{-3} (400 cm^{-3}) and is based on the 30-m K_a-band radar resolution.

the LWC field derived using the radar algorithm in Eq. (1) (see discussion in the next section). All radar data quantities in Fig. 6 are based on 5-s signal averages. It is important to note that, as expected, the strong optical attenuation produced by the water cloud typically limited the useful laser pulse penetration depth to ~200-m, such that the cloud tops could not be observed. A simple lidar algorithm, involving a threshold signal increase maintained over three (18 m) running average data points, was employed to identify the stratus cloud-base altitude. Using this method no significant differences in cloud-base heights were determined at the 0.532- and 1.06-μm lidar channels.

It is clear from Fig. 6a that the lidar-derived cloud base is generally $\leq$50 m lower than the radar-detected height in the presence of Doppler-measured updrafts (negative motions are away from the radar in Fig. 6c), due to the considerably greater sensitivity of optical scattering to the small droplets present near the 100% relative humidity level that traditionally defines cloud base. Where Doppler-derived downdrafts tend to dominate, however, the cloud-base altitudes measured by the radar are in better agreement and may actually be lower than the lidar heights (see especially the consistent downdrafts from 2105 to 2110). This is probably a result of the enhanced ability of the radar to detect the few largest droplets left over from the population during the evaporation process. The presence of cloud regions dominated by evaporative downdrafts, with the associated stronger mixing of dry air aloft, also appears to be related to the upward excursions in both the lidar and radar cloud-base heights.

Unauthenticated | Downloaded 03/29/23 10:44 AM UTC

TABLE 2. Listing of the beginning and ending times; FSSP average droplet concentration N_d; and FSSP-, radar algorithm-derived, and MWR-measured LWP for each aircraft flight segment, including the ascent spiral (S), ramps (R), and fast ramps (FR).

Segment	Time UTC	N_d (cm^{-3})	LWP ($g\ m^{-2}$)		
			FSSP	Radar	MWR
S1	2033:47–2045:24	379	171	236	214
R1	2049:28–2053:44	389	163	259	292
R2	2054:50–2058:15	395	159	192	196
R3	2100:39–2104:35	389	161	230	226
R4	2106:10–2109:07	385	134	182	192
R5	2111:13–2115:25	364	138	164	131
R6	2117:22–2120:40	342	144	194	174
R7	2123:42–2127:59	353	135	155	137
R8	2130:20–2133:13	361	120	156	180
R9	2133:13–2142:16	325	100	133	125
FR1	2142:37–2143:36	242	52.8	71.1	96
FR2	2145:24–2147:52	241	54.7	76.6	95
FR3	2147:52–2149:06	296	64.7	113	91
FR4	2150:56–2152:17	374	81.6	163	133
FR5	2153:10–2154:17	359	83.3	171	170

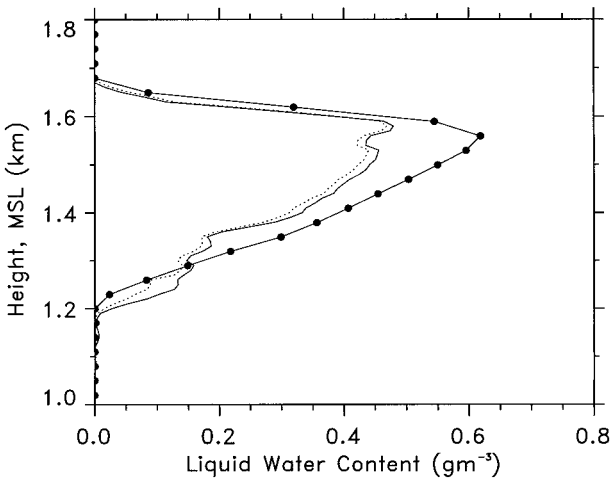

FIG. 4. A five-ramp average (2111–2142) vertical profile of LWC measured by the FSSP (solid), King probe (dotted), and radar-derived (line with dots).

5. Radar-derived cloud products

In this section we show the results of the transformation of the CPRS reflectivity data given in Fig. 6a into fundamental cloud content quantities, such as LWC (Fig. 6d), LWP (Fig. 7), and droplet concentration and mean size (Figs. 8b,c) using retrieval algorithms. Since Eq. (1) has not previously been tested against experimental data, we could begin our analysis by using in situ and MWR data to ''validate'' the radar algorithm. However, this approach assumes that a particular data source is more reliable than another, whereas it must be recognized that the validity of any data intercomparison is subject to basic uncertainties stemming not only from various sources of error but also from experimental realities. For example, in our case the cloud volumes sampled by the zenith-dwelling radar (or MWR) and the wide-ranging aircraft operations are vastly dissimilar, both with respect to the total numbers of particles sampled and the influence of the significant spatial cloud boundary variations revealed in the lidar and radar displays. So, although the general validity of the radar-derived data is shown below, we will put off a detailed assessment to appendix A of the potential impacts imposed by N_d uncertainties and radar calibration errors on radar-derived LWC, as well as the ability of the radar and FSSP to detect both the smallest and largest cloud droplets present.

a. Radar intercomparisons

The radar-derived vertical LWC profiles shown as the solid lines in Fig. 3 have been computed from Eq. (1) using the in situ measured values of N_d for each ramp given in Table 2, and in Fig. 4 from the $N_d = 345\ cm^{-3}$ average of ramps R5–R9. Although the single-ramp intercomparisons reveal discrepancies no doubt reflecting cloud spatial inhomogeneities and aircraft ($\sim$30 m) height uncertainties, several are favorable, particularly for the five selected ramps. However, in general the peaks in both the individual and averaged radar-derived LWC profiles in the upper cloud region tend to exceed the in situ measurements, while the radar values tend to be smaller in the vicinity of cloud base. Moreover, the LWP values in Table 2 show that the in situ values average 80% over the middle five ramps, but only 60% over the last five fast ramps compared to the radar-derived data. Possible reasons for these discrepancies are discussed in appendix A.

As a further test employing an independent source of data, compared in Fig. 7 are the LWP values measured by the MWR (solid line) with the vertically integrated radar LWC values (asterisks, assuming the in situ average $N_d = 347\ cm^{-3}$) over the entire 1.5-h period. It is clear from this intercomparison and the aircraft ramp-average LWP data in Table 2 that the radar versus radiometric results are consistently in good agreement. On the other hand, the open symbols represent each of the ramp-averaged in situ LWP values from Table 2, which, in keeping with the previous discussion, tend to somewhat underestimate those derived via remote sensing.

b. High-resolution cloud structure

It can be concluded from an examination of the high-resolution radar-derived Doppler velocity and LWC fields shown in Figs. 6c,d that the structure of this stratus cloud layer has been depicted at unparalleled resolution. Some cellularity is indicated in the LWC and Doppler velocity fields, but in this graphic form only a poor organization of updrafts and downdrafts is apparent. To better visualize the vertical velocity structure within the cloud, Fig. 9 shows the aircraft-derived velocities collected from 2255 to 2302 during an extended constant-

Unauthenticated | Downloaded 03/29/23 10:44 AM UTC

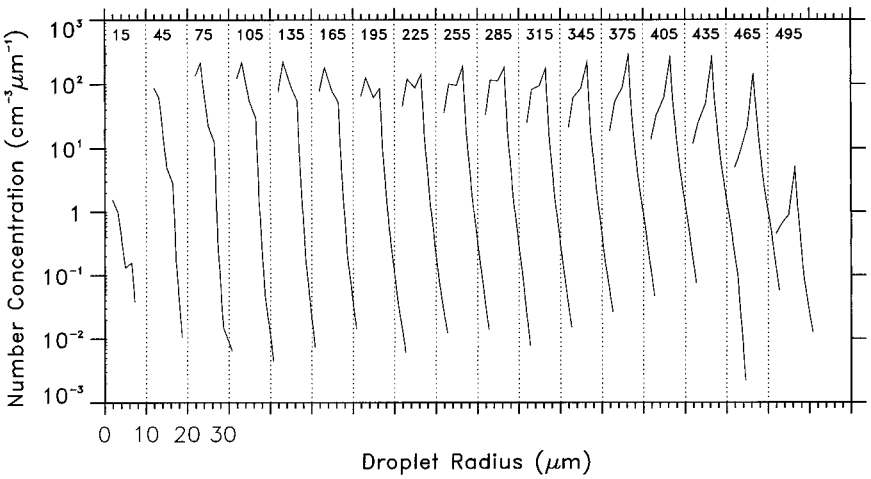

FIG. 5. A typical example (from ramp R7) of the evolution with height (see inserted heights in meters above cloud base) of the FSSP droplet size distribution.

level leg performed at 1.375 km. This plot also shows that the vertical motions varied between ± 1 m s^{-1}, and suggests that both high- and low-frequency variations may be present. Moreover, in Fig. 10 we examined the variability in radar-derived LWC and mean droplet radius (see below) for a constant 1.39-km altitude near the cloud layer center versus time, which is equivalent to ~50-km distance. These data reflect the microphysical consequences of the organizations in vertical velocities, particularly at the longer timescales.

We next show in Fig. 11 the results of frequency analysis of the in situ vertical velocity data in Fig. 9 and the LWC data of Fig. 10b. This analysis suggests an organization of vertical velocities on the order of 0.1 and 10 km, which can most readily be explained by the typical separations between small-scale convective cells and mesoscale cloud bands such as those depicted in the visible satellite imagery near the CART site in Fig. 1b.

c. Droplet concentration and radius

Figure 8 provides 1-min averaged data (corresponding to the available MWR temporal resolution) derived using Eq. (1) and the computed N_d method constrained by the microwave radiometer findings [Eq. (2)] in terms of time–height plots of radar-derived (a) adjusted LWC and (b) mean radius $\bar{r}$, and (c) a scatterplot of N_d values. Note that although the derived N_d vary over a relatively wide range (likely reflecting differences in the cloud volumes sampled by the radar and radiometer in view of their separation), the 1-min data are in reasonable agreement with the ramp-averaged values shown as the open symbols. As a matter of fact, the average of all radar-MWR–derived data points is $N_d = 372$ cm^{-3}, compared to the 347 cm^{-3} obtained by the aircraft. This indicates an acceptable level of insensitivity to some uncertainty in N_d, which is explored in appendix A. Because of the normalization to the LWP data, the radar-derived LWP values would now correspond exactly to the trace measured by the radiometer (the solid line in Fig. 7). In appendix B we consider an alternate approach for deriving LWC using combined radar and MWR data based on a dissimilar method (Frisch et al. 1995), and contrast our results.

Finally, Fig. 8b depicts the time evolution in the vertical structure of radar-derived $\bar{r}$ at the 1-min resolution of the MWR, which tends to show a gradual increase in drop size to near the cloud top, where entrainment causes rapid evaporation. These results from Eq. (3) also show maximum radii of ~9 μm at several cellular locations close to cloud top, but these regions do not always correspond to the highest LWC regions (Fig. 8a). Recall that the LWC and $\bar{r}$ derived for a constant 1.39-km altitude are compared in Fig. 10, which illustrates that although the variations in these two parameters are generally in phase, some noticeable decorrelations exist. It is apparent that the evolution in stratus cloud microphysical content reflects processes governed by time-varying vertical motions and entrainment effects at any particular location.

6. Stratus adiabatic extent

An important stratus property is the extent that cloud content deviates from adiabatic conditions, as is examined in Fig. 12. Although it is straightforward to predict the contents of stratus clouds undergoing adiabatic ascent using 1D models, it is another matter to comprehend the alterations that occur in nonidealistic clouds subject to mixing with environmental air through the entrainment process. Such consequences affect LWC, N_d, and $\bar{r}$, which thus impact the cloud radiative characteristics. A potential difficulty in this analysis, however, lies in establishing where the stratus cloud base actually lies; the FSSP, with a minimum size de-

Unauthenticated | Downloaded 03/29/23 10:44 AM UTC

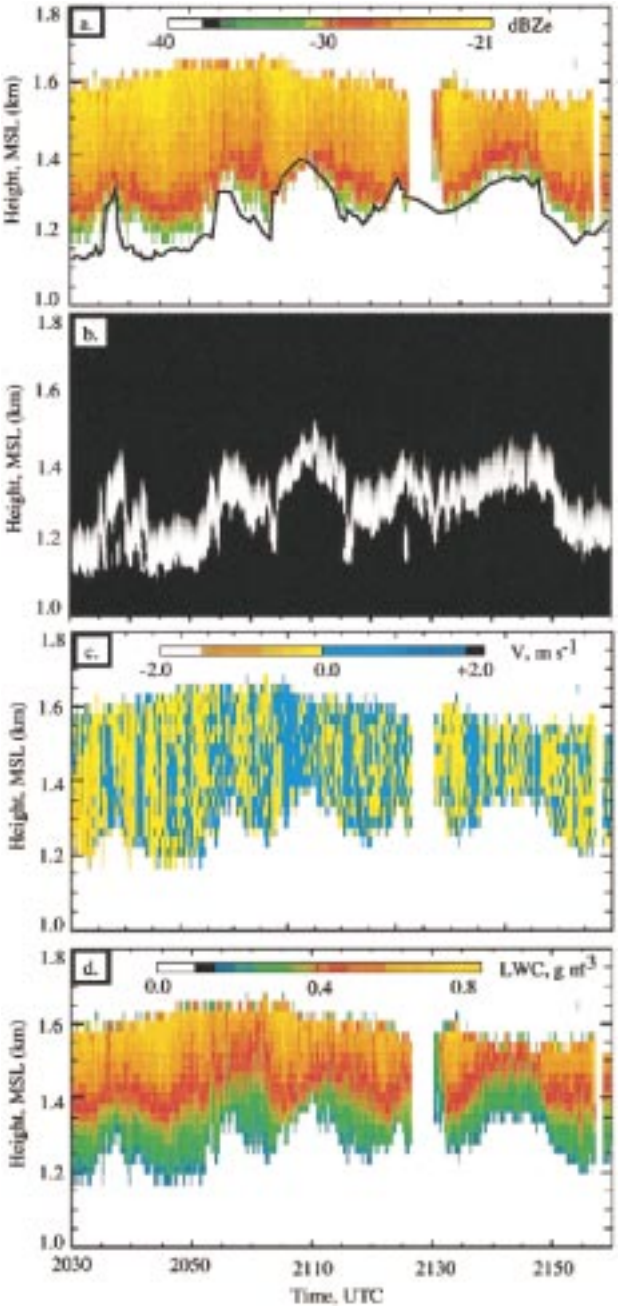

FIG. 6. High-resolution time–height displays of (a) K_a-band radar reflectivity factor Z_e (with lidar cloud-base heights shown by the line), (b) 0.532-μm lidar relative returned energy, (c) mean Doppler radar velocity V, and (d) radar algorithm–derived LWC using $N_d = 347$ cm^{-3}.

tection threshold of ~3-μm diameter, may not sense the actual cloud-base position, while the radar minimum detectable signals certainly prohibit exact cloud-base identification (see appendix A). Moreover, it is difficult to relate the highly resolved (6 m) lidar cloud-base height to the radar or aircraft measurements because of the strength of the observed spatial and temporal cloud

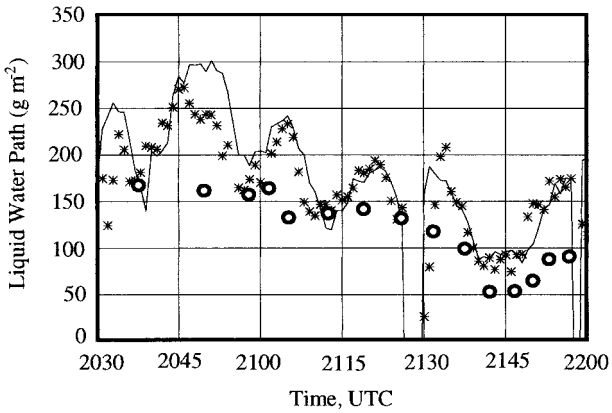

FIG. 7. Comparison of liquid water path LWP measurements derived from the MWR (solid line), the radar algorithm (*) using a constant $N_d = 347$ cm^{-3}, and ramp-integrated FSSP LWC (○).

variations. For the data shown in Fig. 12, we have used the level at which the FSSP LWC first exceeded 0 g m^{-3} in a 10-m height average, in order to estimate cloud-base height. Unfortunately, a similar approach cannot be used for the radar-derived data because of greater uncertainties in cloud-base levels.

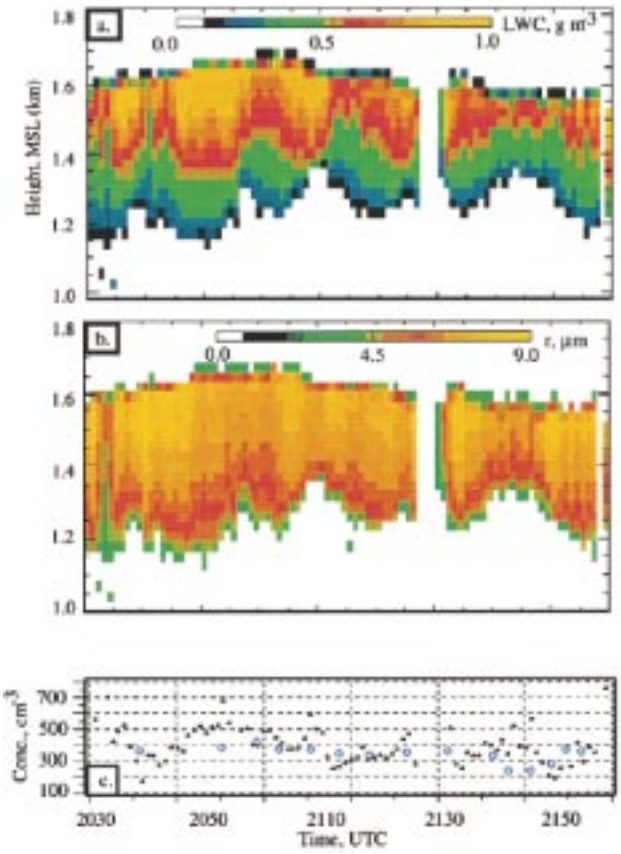

FIG. 8. Comparison of 1-min resolution (a) stratus LWC field using the variable N_d radar algorithm method, (b) radar-derived $\bar{r}$, and (c) a plot of radar-derived (*) and in situ ramp-averaged (○) N_d.

Unauthenticated | Downloaded 03/29/23 10:44 AM UTC

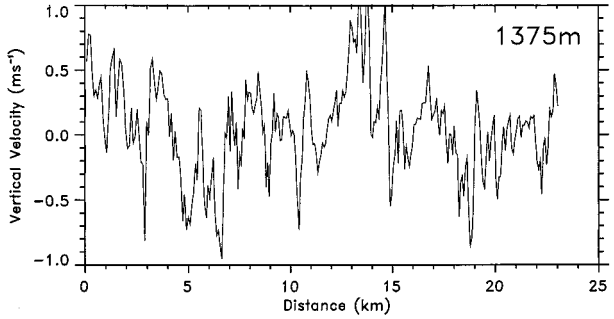

FIG. 9. Vertical velocity vs distance plot for an extended aircraft leg performed at an average height of 1.375 km.

The data in Fig. 12 for all 15 aircraft profiles of LWC and $\bar{r}$ [from Eq. (3)] are compared to curves predicted by our adiabatic cloud model (solid lines), assuming a 0°C cloud-base temperature, $N_d = 347$ cm^{-1}, 0.3 m s^{-1} updraft velocity, and that cloud base corresponds to the model-generated 100% relative humidity level. The 0.3 m s^{-1} ascent rate is based on the average updraft velocity measured by the aircraft using the conditional sampling method during horizontal legs (Fig. 9). It is clear that many LWC profiles are reasonably adiabatic up to a usually narrow cloud-top entrainment zone. The near-adiabatic cloud extent is also reflected in the mean droplet radius profiles, except at higher altitudes where $\bar{r}$ always remains below the adiabatic prediction. The in situ data in Fig. 12b suggest a bifurcation of the $\bar{r}$ profiles below the middle cloud region, perhaps as a result of the sampling of both predominantly ascending and (more mixed) descending cloud parcels.

7. Conclusions

What has emerged from this case study from the April 1994 RSC IOP campaign is a uniquely comprehensive description of the microphysical content and structure of a pure liquid-phase continental stratus cloud layer. The remote and in situ findings described above, along with the lower-atmospheric structure data in Fig. 2, illustrate the characteristic conditions and dynamics associated with the maintenance of a stratus cloud-topped mixed layer, where cloud content is close to adiabatic. The cloud system, which was associated with a springtime cold-air outbreak deep into the southern Great Plains, occurred at the top of a well-mixed, 1.3 km deep boundary layer capped by a strong temperature inversion. The content of this slightly supercooled stratus cloud reflects the continental source of CCN from a reasonably pollution-free region; the aircraft segment-averaged droplet concentrations ranged from 241 to 395 cm^{-3}, and the relatively narrow size distributions and small mean radii of <10 μm were unfavorable for drizzle drop production. Values of radar-derived LWP ranged from 71 to 259 g m^{-2}, depending essentially on cloud physical depth. This last finding is consistent with

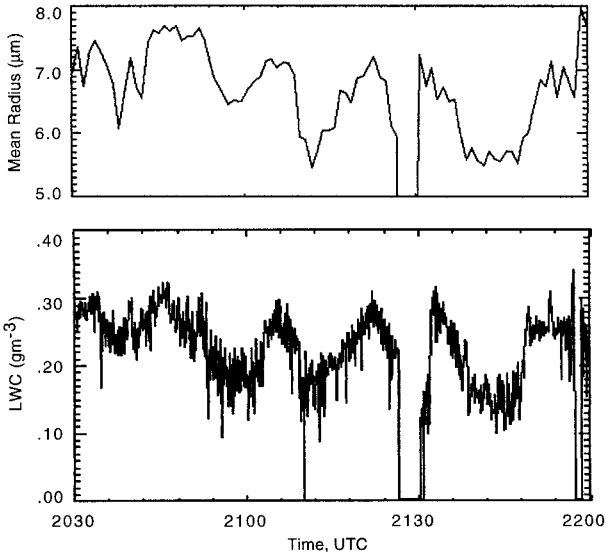

FIG. 10. Variability of radar-derived (top) mean radius $\bar{r}$ at 1-min resolution, and (bottom) LWC at 5-s resolution over the 1.5-h radar observation period, for a constant 1.39-km altitude.

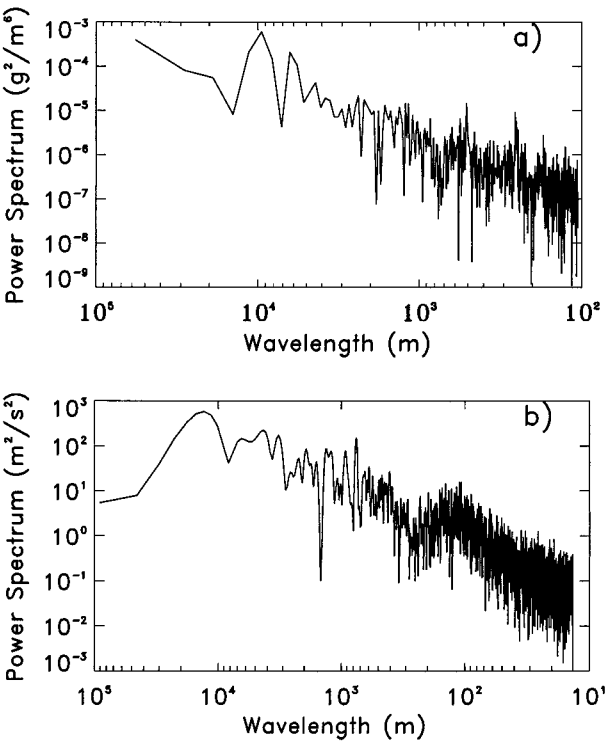

FIG. 11. Comparison of power spectra from (a) radar-derived LWC (Fig. 10b) and (b) aircraft-derived vertical velocity (Fig. 9). The power spectra are derived from 24-Hz recordings of vertical air velocity at the ~120 m s^{-1} Citation true airspeed, or based on 5-s radar signal averages at the 9 m s^{-1} average cloud advection speed.

Unauthenticated | Downloaded 03/29/23 10:44 AM UTC

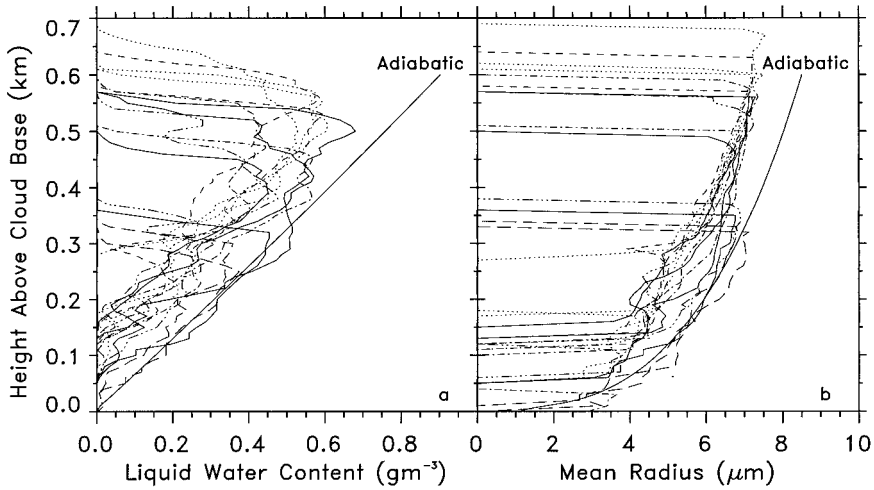

FIG. 12. Vertical profiles of ramp-averaged in situ (left) LWC and (right) $\bar{r}$ profiles compared to appropriate adiabatic model predictions in terms of height above the approximate cloud-base position, indicating the degree of adiabatic cloud content.

the climatological findings reported by Fouquart et al. (1990).

Both Doppler radar and in situ data show frequent vertical motions within the stratus layer of ± 1.0 m s^{-1}, with an average of ± 0.3 m s^{-1} using the conditional sampling method. Frequency analysis of the variations in vertical motions and cloud content parameters like LWC, which preserve the dynamics responsible for cloud maintenance, implies cloud organizations on the orders of 100 m and 10 km. These scales presumably represent the separations between cloud-scale convective cells and mesoscale cloud bands.

Importantly, it has been shown that modern remote sensing methods using cloud model–based algorithms are well suited for determining the microphysical properties of these ubiquitous, but largely overlooked, water clouds. The depth of these findings has been made possible by the application of a radar retrieval algorithm, which compares favorably to a method based on a distinct theoretical approach (appendix B) as well as microwave radiometer and, to a lesser extent, in situ data. Although the aircraft measurements from this experiment have clearly provided a useful view of boundary layer cloud properties over the flight, it is apparent that, in comparison, the multiple remote sensor method has yielded a more comprehensive image of the horizontal and vertical cloud content and structure. Considering the nontraditional nature of the target, a slightly supercooled, nonprecipitating water cloud, this is a powerful illustration of the research capabilities of modern millimeter-wave remote sensors. It is also worth emphasizing that the derived data quantities, which can be routinely monitored with such an instrument ensemble, are of great significance for the assessment of the radiative properties of water clouds. We plan to begin exploiting this radar–MWR algorithm to convert the continuous CART Millimeter Cloud (K_a band) Radar data stream to such data quantities under appropriate conditions.

Acknowledgments. This research has been supported through the Environmental Sciences Division of the U.S. Department of Energy under Grant DEFG-0394ER61747, as part of the Atmospheric Radiation Measurement program, and by NSF Grant ATM-9528287.

APPENDIX A

Experimental Uncertainties

Addressed here are issues related to defining the basic uncertainties in measuring stratus cloud content both with remote sensors and in situ probes. This obviously impacts the validation of the radar retrieval algorithm that is the basis of this case study. We mean validation in the sense that an acceptable level of agreement exists between (imperfect) measurements and/or modeled expectations. Our goal is to account for the differences between the radar- and FSSP-derived LWP and LWC profiles (Fig. 3, Table 2), which could be a result of not only basic errors but also the manner in which the cloud was sampled by the various probes. As mentioned, the great disparity in cloud volumes sensed by the radar (or MWR) and FSSP (or King probe) is a major cause for concern; for example, during a typical ramp the 30-m height interval corresponds to a cloud volume of $\sim 6 \times 10^{-4}$ m^3, in comparison to the 3×10^3 m^3 volume from a *single* radar pulse at 1.0-km range.

We begin with analyses of the effects on the radar-derived LWC profiles of uncertainties in the radar calibration term (Fig. A1) and in specifying the droplet concentration (Fig. A2). In both figures the standards to judge the effects of the errors are the radar and FSSP

Unauthenticated | Downloaded 03/29/23 10:44 AM UTC

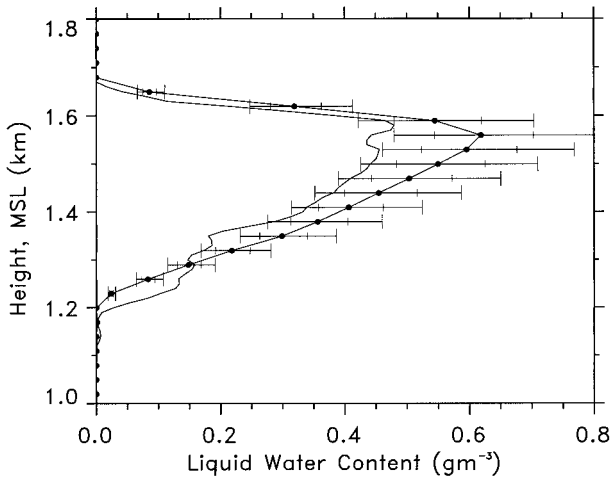

FIG. A1. Error bars in the derived LWC profile produced by uncertainties in the radar calibration constant of ±1 and ±2 dB, compared to average FSSP data from the five middle ramps (R5–R9) during a period of relatively uniform cloud properties.

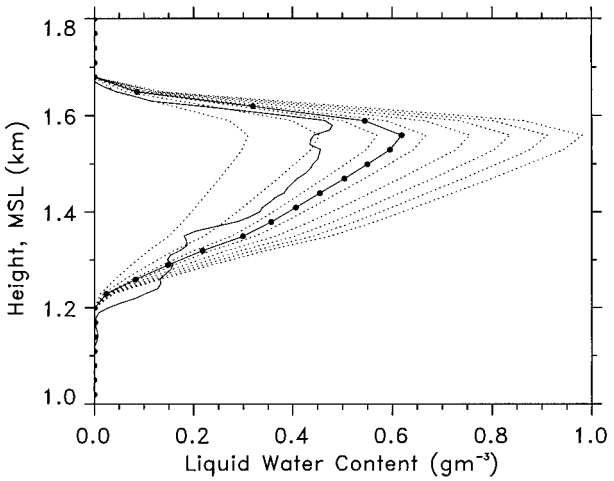

FIG. A2. Analysis of radar-derived LWC errors from uncertainties in guessing (i.e., without surface CCN or in situ support) N_d values within extreme limits (dotted lines, left to right from 100 to 800 cm^{-3}), compared with aircraft data (as in Fig. A1).

profiles from Fig. 4. Figure A1 illustrates that a radar calibration error of ±2 dB, which is the uncertainty limit inherent in the CPRS data, can produce changes in the LWC profile on the order of 25%. Clearly, accurate radar calibration is a necessity for this method. Figure A2 reveals that errors in specifying N_d can lead to significant uncertainties in LWC, unless knowledge of local CCN concentrations is estimated climatologically or measured from the ground.

The analysis in Fig. A3 deals with the uncertainties produced by the radar minimum detectable signal (MDS) on LWP and the detected cloud-base height, by converting the results from the 1D cloud model to radar reflectivity (see figure caption). Obviously, only the most sensitive radars can be used to obtain accurate cloud boundary data under these conditions. We note that the corresponding MDS of the CPRS at 1.0-km range is −35.5 dBZ_e for the 5-s signal average used in Fig. 6. Thus only a small error in LWP and a slight (~50 m) upward shift in the radar cloud-base height would occur. Although not shown in Fig. A3, consideration of the humidity data and the average Z_e profile to compute the K_a-band radar total extinction rate (Liao and Sassen 1994) reveals only a negligible decrease in LWP in our case.

Finally, we consider the effects of the FSSP sampling inefficiencies in terms of the ~3-μm diameter detection threshold, and the undercounting of the largest (and fewest) droplets in the tail of the spectra. Although our model results show that the neglect of small droplets has a negligible effect on LWP, it is more difficult to predict the effects of undersampling the largest droplets in the limited FSSP sample times. It can be seen from Fig. 5 that the minimum detected droplet concentrations in each 30-m height interval vary between 0.1 and 0.01 cm^{-3}. The situation for the fast ramps is worse, since the aircraft remained in cloud for only about one-third the time. (Recall that for ramps R5–R9 and FR1–FR5 the FSSP LWP averaged 80% and 60%, respectively, of the radar values.) Thus, of the various uncertainties that could have affected the remote/in situ data comparison, it appears that the poor sampling efficiency of the FSSP with regard to the few largest droplets present is the best candidate for accounting for the LWP difference. A small (<2 dB) radar calibration error could

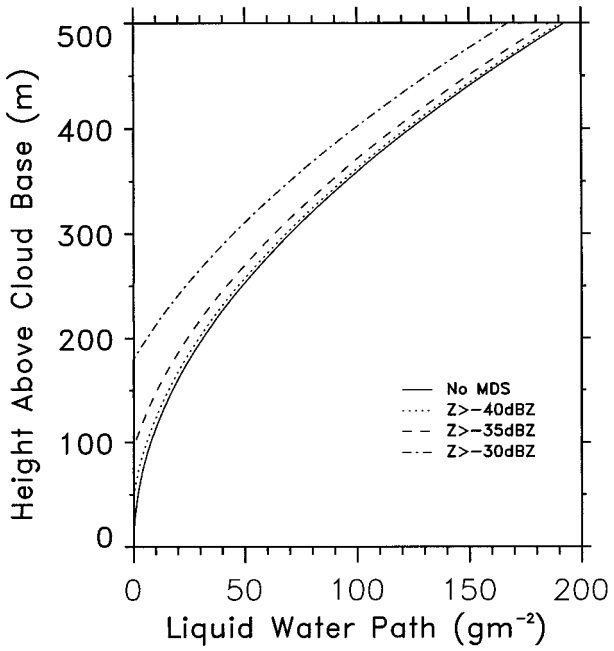

FIG. A3. Parcel cloud model–based analysis of errors in radar-derived LWP due to MDSs between −30 and −40 dBZ_e, compared to an adiabatic result (solid) for a 0°C cloud-base temperature and N_d = 350 cm^{-3}.

Unauthenticated | Downloaded 03/29/23 10:44 AM UTC

also have contributed, but then one must have a compensating MWR error, which was not found. Additionally, as mentioned earlier the radar algorithm does not appear to be very sensitive to nonadiabatic cloud growth conditions, while a comparison of the radar-measured radar reflectivity factors with those computed from the FSSP droplet spectra shows that the latter are ~ -1 to -4 dB less than the radar data, which can also be attributed to FSSP large-droplet undercounting.

These findings obviously have implications for the conduct of stratus cloud research studies; the chief problem is how to accrue an adequate and representative cloud volume in view of inherent cloud variations that occur with time, distance, and height using current in situ probes.

APPENDIX B

Underlying Theory

The combined radar–MWR stratus cloud retrieval research reported here has a previous analogue stemming from K_a-band studies in the eastern Atlantic Ocean during the Atlantic Stratocumulus Transition Experiment experiment (Frisch et al. 1995). This algorithm assumes a lognormal distribution of cloud droplets and relates the sixth moment of the distribuiton (related to Z_e) to the lower-order moments related to the mean size and water content. More recently, Frisch et al. (1999) show that LWC can be derived independently of both the radar calibration and any assumption regarding the distribution width or particle concentration, as long as LWP data are available and the assumption is made that the sixth moment of the particle size distribution is correlated to the third moment (i.e., $\langle r^6 \rangle = k^2 \langle r^3 \rangle^2$, where k is a correlation coeffecient). This argument can be developed as follows (Frisch et al. 1999). The LWC and radar reflectivity can be expressed as

$$\mathrm{LWC} = \frac{4\pi}{3} \rho_w N_d \langle r^3 \rangle, \tag{B1}$$

$$Z_e = 2^6 N_d \langle r^6 \rangle, \tag{B2}$$

which are, respectively, Eqs. (3) and (4) of Frisch et al. (1995). Equation (B2) can be written

$$N_d \langle r^3 \rangle = \frac{N_d^{0.5} Z_e^{0.5}}{8k}. \tag{B3}$$

Substituting Eq. (B3) into (B1) and collecting constant terms, we can write

$$\mathrm{LWC} = \frac{\rho_w N_d^{0.5} Z_e^{0.5}}{k}. \tag{B4}$$

The LWP can be similarly expressed as

$$\mathrm{LWP} = \frac{\rho_w N_d^{0.5}}{k} \int_{z_{cb}}^{z_{ct}} Z_e^{0.5}\, dz. \tag{B5}$$

Combining (B4) and (B5) by eliminating $N_d^{0.5}$ yields

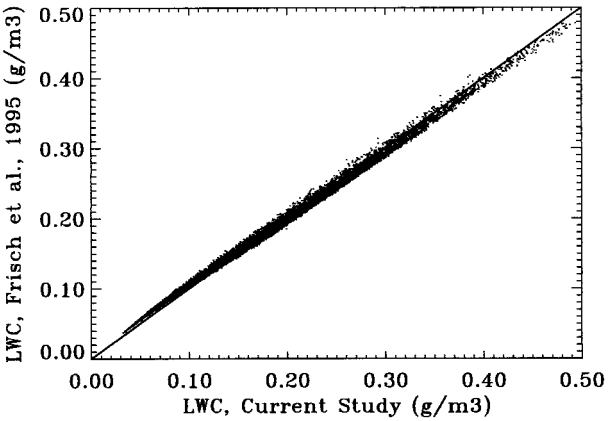

FIG. B1. Scatterplot of LWC values obtained with the current and Frisch et al. (1995) methods using CPRS K_a-band radar and MWR data averaged over 1-min intervals, based on the algorithm given in the text to compute the droplet distribution mean width (averaged over the entire period).

$$\mathrm{LWC} = \frac{\mathrm{LWP} Z_e^{0.5}}{\int_{z_{cb}}^{z_{ct}} Z_e^{0.5}\, dz}. \tag{B6}$$

Using Eq. (1) of the present study, we can write

$$\mathrm{LWC} = \left(\frac{Z_e N_d}{3.6} \right)^{0.56} = 0.49 Z_e^{0.56} N_d^{0.56}, \tag{B7}$$

and LWP can be written similarly, assuming N_d is constant through the cloud depth:

$$\mathrm{LWP} = 0.49 N_d^{0.56} \int_{z_{cb}}^{z_{ct}} Z_e^{0.56}\, dz. \tag{B8}$$

Now, combining Eqs. (B7) and (B8) leads to

$$\mathrm{LWC} = \frac{\mathrm{LWP} Z_e^{0.56}}{\int_{z_{cb}}^{z_{ct}} Z_e^{0.56}\, dz}, \tag{B9}$$

an expression very similar to Eq. (B1). The small difference in the exponents results from a slight deviation of the adiabatic cloud model results (based on measured CCN spectra) from a truly lognormal distribution. As we show in the comparison of results in Fig. B1, this leads to a small deviation in the slope of the regression line from 1:1 and a small amount of scatter in the data points.

REFERENCES

Albrecht, B. A., R. S. Penc, and W. H. Schubert, 1985: An observational study of cloud-topped mixed layers. *J. Atmos. Sci.*, **42,** 800–822.

——, D. A. Randall, and S. Nicholls, 1988: Observations of marine stratocumulus during FIRE. *Bull. Amer. Meteor. Soc.*, **69,** 618–626.

Unauthenticated | Downloaded 03/29/23 10:44 AM UTC

——, C. S. Bretherton, D. Johnson, W. H. Schubert, and A. S. Frisch, 1995: The Atlantic Stratocumulus Transition Experiment—ASTEX. *Bull. Amer. Meteor. Soc.,* **76,** 889–903.

Atlas, D., 1954: The estimation of cloud content by radar. *J. Meteor.*, **11,** 309–317.

Brost, R. A., D. H. Lenschow, and J. C. Wyngaard, 1982: Marine stratocumulus layers. Part I: Mean conditions. *J. Atmos. Sci.,* **39,** 800–817.

Del Genio, A. D., M.-S. Yai, W. Kovari, and K. K.-W. Lo, 1996: A prognostic cloud water parameterization for global climate models. *J. Climate,* **9,** 270–304.

Fouquart, Y., J. C. Buriez, M. Herman, and R. S. Kandel, 1990: The influence of clouds on radiation: A climate-modeling perspective. *Rev. Geophys.,* **28,** 145–166.

Frisch, A. S., C. W. Fairall, and J. B. Snider, 1995: Measurement of stratus cloud and drizzle parameters in ASTEX with K_a-band Doppler radar and microwave radiometer. *J. Atmos. Sci.,* **52,** 2788–2799.

——, G. Feingold, C. W. Fairall, T. Uttal, and J. B. Snider, 1999: On cloud radar and microwave radiometer measurements of stratus liquid water profiles. *J. Geophys. Res.,* in press.

Gultepe, I., and G. A. Isaac, 1997: Liquid water content and temperature relationship from aircraft observations and its applicability to GCMs. *J. Climate,* **10,** 446–452.

Hanel, G., 1972: The ratio of the extinction coefficient to the mass of atmospheric aerosol particles as a function of the relative humidity. *Aerosol Sci.,* **3,** 455–460.

Hogg, D. C., F. O. Guiraud, J. B. Snider, M. T. Decker, and E. R. Westwater, 1983: A steerable dual-channel microwave radiometer for measurements of water vapor and liquid in the troposphere. *J. Climate Appl. Meteor.,* **22,** 789–806.

Kogan, Z. N., Y. L. Kogan, and D. K. Lilly, 1996: Evaluation of sulfate aerosols indirect effect in marine stratocumulus clouds using observation-derived cloud climatology. *Geophys. Res. Lett.,* **23,** 1937–1940.

Lhermitte, R., 1987: A 94-GHz Doppler radar for cloud observations. *J. Atmos. Oceanic Technol.,* **4,** 36–48.

Liao, L., and K. Sassen, 1994: Investigation of relationships between K_a-band radar reflectivity and ice and liquid water contents. *Atmos. Res.*, **34,** 231–248.

Martin, G. M., D. W. Johnson, and A. Spice, 1994: The measurement and parameterization of effective radius of droplets in warm stratocumulus clouds. *J. Atmos. Sci.,* **51,** 1823–1842.

Mead, J. B., A. L. Pazmany, S. M. Sekelsky, and R. E. McIntosh, 1994: Millimeter-wave radar for remotely sensing clouds and precipitation. *Proc. IEEE,* **82,** 1891–1906.

Pasqualucci, F., B. Bartram, R. A. Kropfli, and W. R. Moninger, 1983: A millimeter-wavelength dual-polarization Doppler radar for cloud and precipitation studies. *J. Climate Appl. Meteor.,* **22,** 758–765.

Sassen, K., 1994: Advances in polarization diversity lidar for cloud remote sensing. *Proc. IEEE,* **82,** 1907–1914.

——, and L. Liao, 1996: Estimation of cloud content by W-band radar. *J. Appl. Meteor.,* **35,** 932–938.

——, H. Zhao, and G. C. Dodd, 1992: Simulated polarization diversity returns from water and precipitating mixed phase clouds. *Appl. Opt.,* **31,** 2914–2923.

Sauvageot, H., and J. Omar, 1987: Radar reflectivity of cumulus clouds. *J. Atmos. Oceanic Technol.,* **4,** 264–272.

Slingo, A., 1990: Sensitivity of the earth's radiation budget to changes in low clouds. *Nature,* **343,** 49–52.

Stokes, G. M., and S. E. Schwartz, 1994: The Atmospheric Radiation Measurement (ARM) program: Programmatic background and design of the cloud and radiation testbed. *Bull. Amer. Meteor. Soc.,* **75,** 1201–1221.

Twomey, S., 1974: Pollution and the planetary albedo. *Atmos. Environ.,* **8,** 1251–1256.

Unauthenticated | Downloaded 03/29/23 10:44 AM UTC